entropy

Article

Four-Objective Optimization for an Irreversible Porous Medium Cycle with Linear Variation in Working Fluid's Specific Heat

Pengchao Zang [1,2,3], Lingen Chen [1,2,3,*], Yanlin Ge [1,2,3], Shuangshuang Shi [1,2,3] and Huijun Feng [1,2,3]

1. Institute of Thermal Science and Power Engineering, Wuhan Institute of Technology, Wuhan 430205, China; zangpengchaoy@163.com (P.Z.); geyali9@hotmail.com (Y.G.); shishuangshuang20@163.com (S.S.); huijunfeng@139.com (H.F.)
2. Hubei Provincial Engineering Technology Research Center of Green Chemical Equipment, Wuhan 430205, China
3. School of Mechanical & Electrical Engineering, Wuhan Institute of Technology, Wuhan 430205, China

* Correspondence: lingenchen@hotmail.com

Abstract: Considering that the specific heat of the working fluid varies linearly with its temperature, this paper applies finite time thermodynamic theory and NSGA-II to conduct thermodynamic analysis and multi-objective optimization for irreversible porous medium cycle. The effects of working fluid's variable-specific heat characteristics, heat transfer, friction and internal irreversibility losses on cycle power density and ecological function characteristics are analyzed. The relationship between power density and ecological function versus compression ratio or thermal efficiency are obtained. When operating in the circumstances of maximum power density, the thermal efficiency of the porous medium cycle engine is higher and its size is less than when operating in the circumstances of maximum power output, and it is also more efficient when operating in the circumstances of maximum ecological function. The four objectives of dimensionless power density, dimensionless power output, thermal efficiency and dimensionless ecological function are optimized simultaneously, and the Pareto front with a set of solutions is obtained. The best results are obtained in two-objective optimization, targeting power output and thermal efficiency, which indicates that the optimal results of the multi-objective are better than that of one-objective.

Keywords: irreversible porous medium cycle; linear variable specific; power density; ecological function; multi-objective optimization; finite time thermodynamics

check for updates

Citation: Zang, P.; Chen, L.; Ge, Y.; Shi, S.; Feng, H. Four-Objective Optimization for an Irreversible Porous Medium Cycle with Linear Variation in Working Fluid's Specific Heat. *Entropy* **2022**, *24*, 1074. https://doi.org/10.3390/e24081074

Academic Editors: Brian Agnew and Zi Qian

Received: 27 June 2022
Accepted: 28 July 2022
Published: 3 August 2022

1. Introduction

Finite time thermodynamics (FTT) [1–11] has been made significant progress in the research of thermal cycles and processes, including optimal configurations [12–21] and optimal performances [22–32]. The FTT studies of internal combustion engine cycles mostly focus on the following factors [33]: the effects of different loss models such as heat transfer loss (HTL) [34], friction loss (FL) [35] and internal irreversibility loss (IIL) [36] on the performances of cycles; the effects of power output (P) and thermal efficiency (η) [37], efficient power (Ep) [38], ecological function (E) [39], power density (P_d) [40] and other objective extreme values on the optimal performances of cycles; the effects of different working fluid (WF)-specific heat (SH) models on the performance of cycles, such as the constant SH of WF [41], the linear variable SH of WF [42] and the nonlinear variable SH of WF [43]; and the influence of WF quantum characteristics [44] and performance characteristics of universal cycle [45].

Many scholars have studied the P, η and Ep objective functions of the heat engine cycles. Diskin and Tartakovsky [46] combined electrochemical and Otto cycles, and studied the η characteristic relationship in the circumstances of maximum P. Wang et al. [47]

investigated the P and η of Lenoir cycle. Bellos et al. [48] derived the η of a solar-fed organic Rankine cycle with reheating, which is more efficient than the conventional organic Rankine cycle. Gonca and Hocaoglu [49] investigated the Ep, Ep density and effective η of a Diesel–Miller cycle, considering the influences of compression ratio, pressure ratio and stroke ratio under the condition of variable SH of WF. Gonca and Sahin [50,51] combined the Miller cycle and the Takemura cycle, and derived the P, η, Ep, effective P_d, exergy destruction, exergy efficiency and ecological coefficient of the Miller–Takemura cycle.

Angulo-Brown et al. [52] first put forward the E as optimization objective (OO) in 1991 for heat engines. Yan [53] corrected E. Chen et al. [54] provided a unified definition of E for heat engines, refrigerators and heat pumps. Gonca and Genc [55] investigated the E, P_d, power generation and density of power generation of a gas–mercury–steam system. Jin et al. [56] optimized E performance of an irreversible recompression S-CO_2 cycle and analyzed the influence of the mass flow rate, pressure ratio and diversion coefficient on E performance. Some researchers studied E performances for Brayton [38], diesel [57], Atkinson [58] and dual [59] as well as other cycles.

Sahin et al. [60] proposed the P_d as OO for the first time and introduced it into the performance optimization of the reversible Joule-Brayton cycle. The numerical results show that the design parameters in the circumstances of maximum P_d will result in smaller dimensions, higher η compared to maximum P circumstances. Al-Sarkhi et al. [61] investigated the P_d characteristics of a Miller cycle when any loss does not need to be considered. With the P_d as the OO, Gonca and Genc [62] optimized the double-reheat Rankine cycle which was based on a mercury turbine system. Gonca et al. [63] investigated the influence of the parameters, such as cycle intake temperature, intake pressure, pressure ratio and compression ratio, on the P, P_d and exergy efficiency of a Dual-Diesel cycle. Gonca and Sahin [64] studied cycle P, P_d, ecological coefficient and effective ecological P_d performances of a modified Dual cycle. Subsequently, the OO of P_d [65–67] has been utilized in the performance research and optimizations of heat engines.

With the increase in OOs, there are contradictions among different OOs. To select the optimal result under the coexistence of multiple OOs, many scholars have carried out multi-objective optimization (MOO) [68–77] by NSGA-II [78]. Li et al. [68] established a regenerative Brayton cycle model and carried out MOO on the P, η and dimensionless thermal economic performance. Chen et al. [69] conducted MOO research on an irreversible modified closed Brayton cycle with four OOs of P, η, P_d and E. Fergani et al. [70] performed MOO on the cyclohexane, toluene and benzene of an organic Rankine cycle using a multi-objective particle swarm optimizer. Teng et al. [71] performed MOO on the multiple systems under the conditions of different heat source temperatures of an organic Rankine cycle. Baghernejad et al. [72] took exergy efficiency, overall cost rate and exergy unit cost of generated electricity as OOs, and performed MOO on the combined Brayton and Rankine cycle. Xie et al. [73] performed MOO on the molar flow rate, reactor lengths and inlet temperatures of Braun-type exothermic reactor for ammonia synthesis. Shi et al. [74] and Ge et al. [75] used P, η, P_d and E as OOs and performed MOO for the diesel [74], dual [75] and MHD [76] cycles.

Ferrenberg [79] first proposed a porous medium (PM) engine in 1990 and presented it as a regenerative engine. PM engine is a new type of engine based on PM combustion technology. Xie [80] introduced the super-adiabatic combustion technology in PM into the engine field and studied the characteristics of super-adiabatic combustion under reciprocating flow in PM. Waclas [81] divided the process of injecting high-pressure fuel into the PM body into four parts and proposed the idea of developing a low-emission engine. Durst and Weclas [82] modified a single-cylinder air-cooled diesel engine and proposed a design scheme for a PM engine. Generally, there are two working modes: one is the periodic contact between the PM and the cylinder, and the other is the permanent contact between the PM and the cylinder. PM engine has a larger internal surface area than other engines and are more capable of absorbing and storing heat. Compared with traditional gasoline or diesel engines, PM engines had higher η, lower emissions and higher P. Liu et al. [83]

established the PM engine model with classical thermodynamic theory, and calculated the influence of compression ratio, pre-expansion ratio, pre-pressure ratio on the η and work output of the PM engine. Zhao et al. [84] investigated the effects of initial temperature, structure and injection duration on engine compression ignition in a methane-powered PM engine.

As one of the thermodynamic cycles, the PM cycle has constant volume processes in both endothermic and exothermic processes, similar to the Otto cycle. Liu et al. [85] first applied FTT theory to investigate P and η of an endoreversible PM cycle. Ge et al. [86] studied the P and η of an irreversible PM cycle. The PM cycle can be changed to the Otto cycle when the pre-expansion ratio is 1. Zang et al. [87] studied the P_d performance and performed MOO of the P, η, P_d and E of an irreversible PM cycle.

The previous research of PM cycles assumed that the SH of the WF remained constant during the cycle, but in the actual cycle, the SH of the WF is constantly changing during the functioning of the heat engine. In this paper, based on Ref. [86], an irreversible PM cycle model will be established based on the linear change in SH of the working fluid with its temperature [88], and the FTT theory will be applied to further study the performance of P_d and E. The η, $\overline{P}$, $\overline{P}_d$ and $\overline{E}$ of the irreversible PM cycle will be optimized by MOO, and the optimal result with the smallest deviation index (DI) will be obtained.

2. Model of an Irreversible PM Cycle

The working process of the PM engine is shown in Figure 1a, and the PM combustion chamber is installed on the top of the cylinder. Fresh air enters the cylinder, at this time the PM chamber is isolated from the cylinder, and the PM chamber is fuel vapor. At the end of the intake process, the starter continues to drive the crankshaft to rotate, and the piston moves from bottom to top. At the same time, the PM chamber is closed, and the gas sucked into the cylinder by the intake stroke is enclosed in a closed space. The gas in the cylinder is compressed and the temperature and pressure are getting higher and higher At the end of the compression process, the valve of the PM chamber is opened, and the compressed air enters the PM chamber for instant recuperation, and the recuperation process is approximately a constant volume process. Air and fuel vapor are rapidly mixed in the PM chamber and self-ignited. The heat released during the combustion process is partly stored in the PM chamber and partly driven by the piston to do work, and the combustion process is approximately an isothermal endothermic process. At the end of the adiabatic expansion stroke, the PM chamber valve is closed. After the constant volume exhaust stroke, the intake stroke of a new cycle begins.

An irreversible PM cycle shown in Figure 1b,c: 1–2s is a reversible adiabatic compression process, 1–2 is an irreversible adiabatic compression process; 2 –3 is a constant volume heat recovery process; 3–4 is an isothermal endothermic process; 4–5s is an reversible process of adiabatic expansion, 4–5 is an irreversible process of adiabatic expansion; and 5–1 is constant volume exothermic process.

In the actual cycle, the SH of the WF is constantly changing during the functioning of the heat engine. According to Ref. [88], when the working temperature of the heat engine is between 300–2200 K, the SH of the WF changes linearly with its temperature, and the constant volume SH of the WF is

$$C_v = b_v + KT \tag{1}$$

where b_v and K are constants.

The cycle temperature ratio (τ), pre-expansion ratio (ρ) and compression ratio (γ) are defined as

$$\tau = T_3/T_1 \tag{2}$$

$$\rho = V_4/V_3 \tag{3}$$

$$\gamma = V_1/V_2 \tag{4}$$

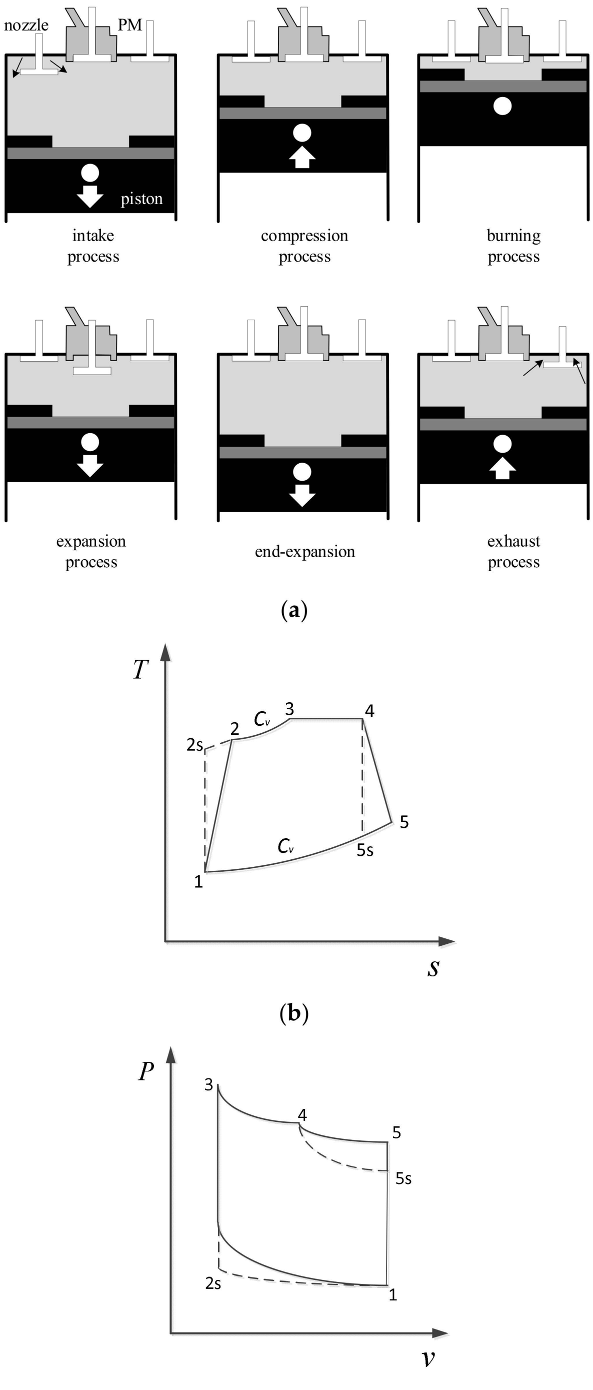

Figure 1. Model of PM cycle. (**a**) Working process of the PM engine. (**b**) T–s graphic. (**c**) P–v graphic.

For processes 1–2 and 4–5, the IIL due to friction, turbulence and viscous stress of the cycle is represented by the compression and expansion efficiency:

$$\eta_c = (T_{2S} - T_1)/(T_2 - T_1) \tag{5}$$

$$\eta_e = (T_5 - T_4)/(T_{5S} - T_4) \tag{6}$$

Because the WF's SH fluctuates with temperature, according to Ref. [88], it is assumed that the process can be decomposed into an infinite number of infinitesimal processes. For each infinitesimal process, it can be approximated that the SH is constant, adding all the infinitesimal processes together constitutes the entire adiabatic process, and any reversible adiabatic process between states i and j may be considered a reversible adiabatic process with infinitely small adiabatic exponent k as a constant. When the temperature and specific volume of the WF change by dT and dV, the following formula can be obtained

$$TV^{k-1} = (T + dT)(V + dV)^{k-1} \tag{7}$$

According to Equation (7), one has

$$K(T_j - T_i) + b_v \ln(T_j / T_i) = -R \ln(V_j / V_i) \tag{8}$$

According to the processes $1 \to 2s$ and $4 \to 5s$, one has

$$K(T_{2s} - T_1) + b_v \ln(T_{2s} / T_1) = R \ln \gamma \tag{9}$$

$$K(T_{5s} - T_4) + b_v \ln(T_{5s} / T_4) = -R \ln(\gamma / \rho) \tag{10}$$

The heat absorption rate of WF is

$$\dot{Q}_{in} = M(\int_{T_2}^{T_3} C_v dT + RT_3 \ln \rho) = M[b_v(T_3 - T_2) + 0.5K(T_3^2 - T_2^2) + RT_3 \ln \rho] \tag{11}$$

The heat release rate of WF is

$$\dot{Q}_{out} = M \int_{T_1}^{T_5} C_v dT = M \int_{T_1}^{T_5} (b_v + KT) dT = M[b_v(T_5 - T_1) + 0.5K(T_5^2 - T_1^2)] \tag{12}$$

where M is the mass flow rate.

In an actual PM cycle, there is HTL between the WF and the cylinder. According to Ref. [13], the HTL rate is defined as

$$\dot{Q}_{leak} = A - \dot{Q}_{in} = (B/2)(T_2 + T_3 - 2T_0) = (T_2 + T_3 - 2T_0)B_1 \tag{13}$$

where A represents the fuel exothermic rate, T_0 represents ambient temperature and $B = 2B_1$ represents the HTL coefficient.

The FL needs to be considered in an actual PM cycle. According to Ref. [35], the FL is a linear function of speed. The power dissipated by FL is

$$P_\mu = 4\mu(4Ln)^2 = 64\mu(Ln)^2 \tag{14}$$

where n represents the rotational speed and L represents the stroke length.

The cycle P and η are

$$\begin{aligned} P &= Q_{in} - Q_{out} - P_\mu \\ &= M[b_v(T_1 + T_3 - T_2 - T_5) + 0.5K(T_1^2 + T_3^2 - T_2^2 - T_5^2) + RT_3 \ln \rho] - 64\mu(Ln)^2 \end{aligned} \tag{15}$$

$$\begin{aligned} \eta &= \frac{P}{Q_{in} + Q_{leak}} \\ &= \frac{M[b_v(T_1+T_3-T_2-T_5)+0.5K(T_1^2+T_3^2-T_2^2-T_5^2)+RT_3 \ln \rho]-64\mu(Ln)^2}{M[b_v(T_3-T_2)+0.5K(T_3^2-T_2^2)+RT_3 \ln \rho]+MB[T_2+T_3-2T_0]} \end{aligned} \tag{16}$$

According to Ref. [89], the volume of total cycle, stroke and clearance are, respectively, as follows:

$$v_t = v_s + v_c \tag{17}$$

$$v_s = \pi d^2 L / 4 \tag{18}$$

$$v_c = \pi d^2 L / [4(\gamma - 1)] \tag{19}$$

According to Ref. [60], the P_d is defined as

$$P_d = P/v_{max} = P/v_1 = 4(\gamma-1)M[C_v(T_3+T_1-T_2-T_5)+RT_3\ln\rho]/(\pi d^2 L\gamma) \quad (20)$$

The entropy generation rates due to FL, HTL, IIL and exhaust stroke are, respectively:

$$\sigma_q = B_1(T_2+T_3-2T_0)[1/T_0-2/(T_2+T_3)] \quad (21)$$

$$\sigma_\mu = \frac{P_\mu}{T_0} = \frac{64\mu(Ln)^2}{T_0} \quad (22)$$

$$\sigma_{2S\to2} = MC_v\ln\frac{T_2}{T_{2S}} = MC_v\ln\frac{T_2}{\eta_c(T_2-T_1)+T_1} \quad (23)$$

$$\sigma_{5S\to5} = MC_v\ln\frac{T_5}{T_{5S}} = MC_v\ln\frac{\eta_e T_5}{T_5+(\eta_e-1)T_4} \quad (24)$$

$$\sigma_{pq} = M\int_{T_1}^{T_5} C_v dT(\frac{1}{T_0}-\frac{1}{T}) = M[\frac{C_v(T_5-T_1)}{T_0}-C_v\ln\frac{T_5}{T_1}] \quad (25)$$

The total entropy generation rate is

$$\begin{aligned}\sigma &= \sigma_q+\sigma_\mu+\sigma_{2S\to2}+\sigma_{5S\to5}+\sigma_{pq}\\ &= [MB(T_2+T_3-2T_0)+64\mu(Ln)^2]/T_0\\ &+M[C_{v2S\to2}\ln(T_2/T_{2S})+C_{v5S\to5}\ln(T_5/T_{5S})]\\ &+M\{[b_v(T_5-T_1)/T_0]-b_v\ln(T_5/T_1)+0.5K(T_5^2-T_1^2)/(2T_0)-K(T_5-T_1)\}\end{aligned} \quad (26)$$

In Equation (26), the temperature in constant volume SH ($C_{v2S\to2}$) is $T=\frac{T_2-T_{2S}}{\ln(T_2/T_{2S})}$, and the temperature in constant volume SH ($C_{v5S\to5}$) is $T=\frac{T_5-T_{5S}}{\ln(T_5/T_{5S})}$.

The cycle E is

$$\begin{aligned}E &= P-T_0\sigma\\ &= M[b_v(T_1+T_3-T_2-T_5)+0.5k(T_1^2+T_3^2-T_2^2-T_5^2)+RT_3\ln\rho]\\ &-MB(T_2+T_3-2T_0)(1-2T_0/(T2+T3))-128\mu(Ln)^2\\ &-MT_0[C_{v2S\to2}\ln(T_2/T_{2S})+C_{v5S\to5}\ln(T_5/T_{5S})]-M[b_v(T_5\\ &-T_1)-b_vT_0\ln(T_5/T_1)+0.5K(T_5^2-T_1^2)-T_0K(T_5-T_1)]\end{aligned} \quad (27)$$

In the actual cycle, the state 3 must be between states 2 and 4, so ρ should satisfy:

$$1 \le \rho \le V_4/V_2 \quad (28)$$

According to Ref. [86], PM cycle converts to the Otto cycle when $\rho=1$, and the P, η, P_d, and E expressions of the Otto cycle can be derived from Equations (15), (16), (20) and (27).

The P, P_d and E after dimensionless treatment are, respectively:

$$\overline{P} = P/P_{\max} \quad (29)$$

$$\overline{P}_d = P_d/(P_d)_{\max} \quad (30)$$

$$\overline{E} = E/E_{\max} \quad (31)$$

Given the γ, the initial temperature T_1, the ρ, the maximum cycle temperature T_4, the η_c and η_e, the Equation (9) can be used to solve T_{2S}. Then solve T_2 from Equation (5), solve T_{5S} from Equation (10), and finally solve T_5 from Equation (6). By substituting the solved T_2 and T_5 into Equations (15), (16), (20) and (27), you can obtain the corresponding P, η, P_d and E.

3. Power Density and Ecological Functions Analyses and Optimizations

The parameters are determined according to Refs. [75,86]: $\rho = 1.2$, $\tau = 5.78 \sim 6.78$, $b_v = 19.868$–23.868 J/mol·K, $k_1 = 0.003844$–0.009844 J/mol·K^2, $T_0 = 300$ K, $T_1 = 350$ K, $\mu = 1.2$ kg/s, $\dot{M} = 1$ mol/s, $B = 2.2$ W/K, $L = 0.07$ m and $n = 30$ s^{-1}.

3.1. Power Density Analyses and Optimizations

Figure 2 shows the effects of τ and ρ on the $\overline{P}_d$ and γ ($\overline{P}_d - \gamma$) as well as the $\overline{P}_d$ and η ($\overline{P}_d - \eta$) characteristics. The curve of $\overline{P}_d - \gamma$ is parabolic-like one, and the $(\overline{P}_d)_{\max}$ corresponds to a optimal γ ($\gamma_{\overline{P}_d}$). The curve of $\overline{P}_d - \eta$ is loop-shaped one which starts from the origin and back to the origin, and there are operating points of $(\overline{P}_d)_{\max}$ and maximum η ($\eta_{\max}$) in the cycle.

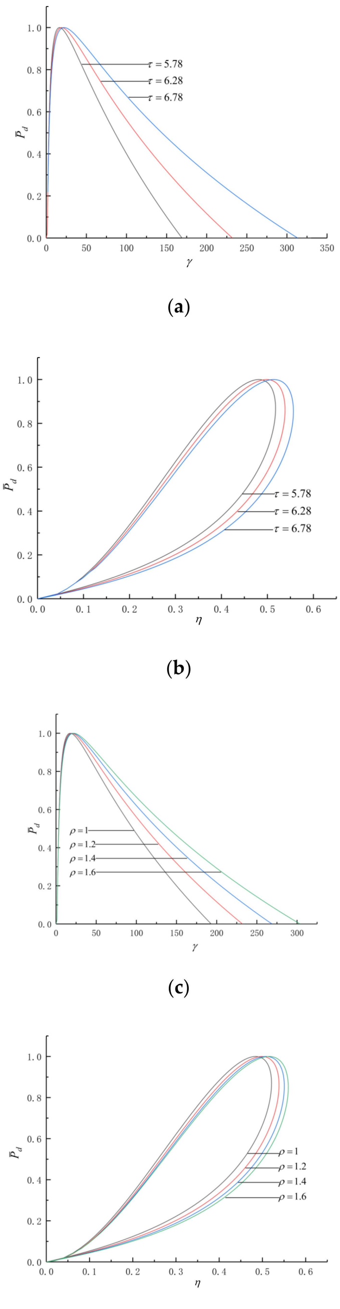

(**a**) (**b**) (**c**) (**d**)

Figure 2. The effects of τ and ρ on $\overline{P}_d - \gamma$ and $\overline{P}_d - \eta$. (**a**) Effect of τ on $\overline{P}_d - \gamma$. (**b**) Effect of τ on $\overline{P}_d - \eta$. (**c**) Effect of ρ on $\overline{P}_d - \gamma$. (**d**) Effect of ρ on $\overline{P}_d - \eta$.

As seen in Figure 2a,b, as τ grows, both $\gamma_{\overline{P}_d}$ and $\eta_{\overline{P}_d}$ get larger. When τ grows from 5.78 to 6.78, $\gamma_{\overline{P}_d}$ grows from 16.5 to 22.3, $\eta_{\overline{P}_d}$ grows from 0.4809 to 0.5139 and $\eta_{\overline{P}_d}$ grows by about 6.86%. As seen in Figure 2c,d, as ρ grows, both $\gamma_{\overline{P}_d}$ and $\eta_{\overline{P}_d}$ get larger. When ρ grows from 1.2 to 1.6, $\gamma_{\overline{P}_d}$ grows from 19.3 to 21.9, $\eta_{\overline{P}_d}$ grows from 0.4986 to 0.5154 and $\eta_{\overline{P}_d}$ grows by about 3.37%. With the increase in the temperature ratio and pre-expansion ratio, the compression ratio and thermal efficiency in the circumstances of maximum dimensionless power density increase. In Figure 2, $\rho = 1$ is the performance characteristics of the Otto cycle. Obviously, the PM cycle has a higher η than the Otto cycle.

Figure 3 shows the $\overline{P}_d - \gamma$ and $\overline{P}_d - \eta$ curves with varying losses and SH characteristics.

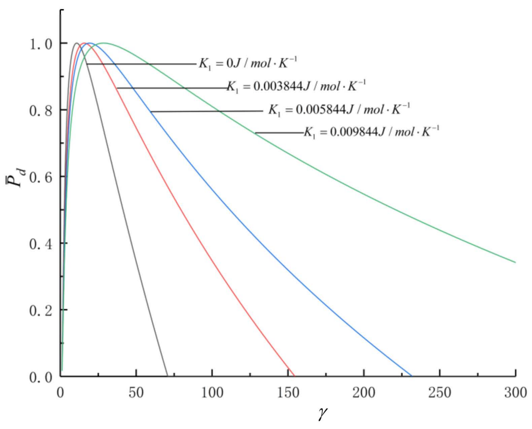

(**a**)

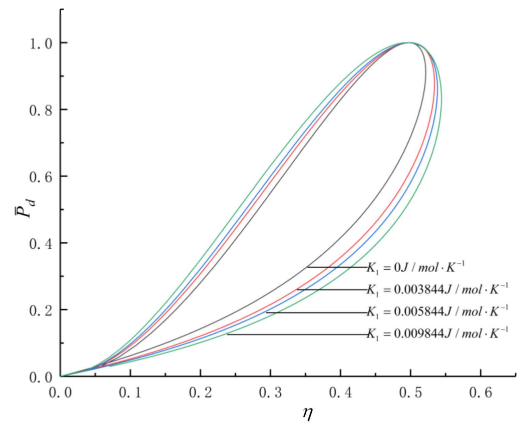

(**b**)

Figure 3. *Cont*.

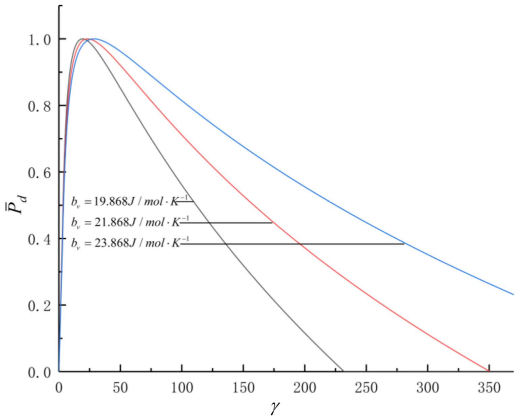

(**c**)

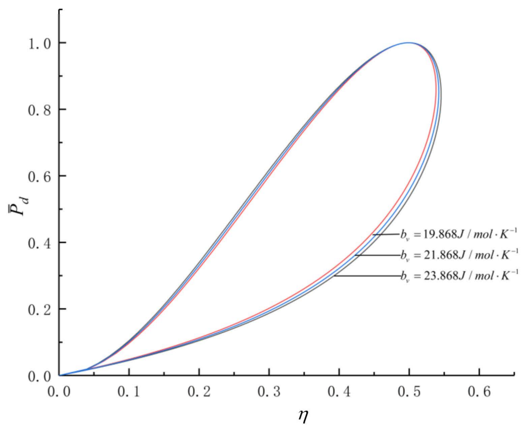

(**d**)

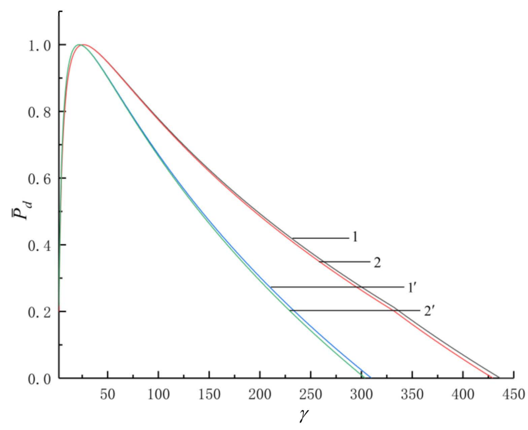

(**e**)

Figure 3. *Cont.*

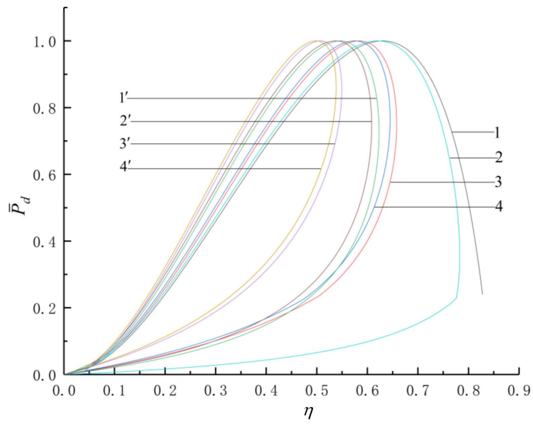

(**f**)

Figure 3. The effects of k_1 b_v B μ η_c and η_e on $\overline{P}_d - \gamma$ and $\overline{P}_d - \eta$. (**a**) Effect of k_1 on $\overline{P}_d - \gamma$. (**b**) Effect of k_1 on $\overline{P}_d - \eta$. (**c**) Effect of b_v on $\overline{P}_d - \gamma$. (**d**) Effect of b_v on $\overline{P}_d - \eta$. (**e**) $\overline{P}_d - \gamma$. (**f**) $\overline{P}_d - \eta$.

Figure 3a,b show the effects of k_1 on $(\overline{P}_d - \gamma)$ and $(\overline{P}_d - \eta)$ characteristics. The degree of variation in the SH of the WF with temperature is represented by k_1. The larger the k_1, the larger the variation range of the SH. As k_1 grows, $\gamma_{\overline{P}_d}$ grows and $\eta_{\overline{P}_d}$ declines. When $k_1 = 0$, the cycle WF is constant SH. When k_1 grows from 0.003844 J/mol·K^2 to 0.009844 J/mol·K^2, $\gamma_{\overline{P}_d}$ grows from 15.8 to 28.4, $\eta_{\overline{P}_d}$ declines from 0.4992 to 0.4949, a decline of 0.86%. Figure 3c,d show the effects of b_v on $\overline{P}_d - \gamma$ and $\overline{P}_d - \eta$ characteristics. As b_v grows, both $\gamma_{\overline{P}_d}$ and $\eta_{\overline{P}_d}$ will become larger. When b_v grows from 19.868 J/mol·K to 23.868 J/mol·K, $\gamma_{\overline{P}_d}$ grows from 19.3 to 28.4, $\eta_{\overline{P}_d}$ grows from 0.4986 to 0.4993 and $\eta_{\overline{P}_d}$ grows by about 0.14%. As seen in Figure 3e,f, when only FL exists, comparing curves 1 and 2, as μ grows from 0 kg/s to 1.2 kg/s, $\gamma_{\overline{P}_d}$ is nearly unchanged, and $\eta_{\overline{P}_d}$ declines from 62.95% to 62.03%, a decline of 1.46%. When IIL exists only, comparing curves 1 and 1′, as η_c and η_e declines from 1 to 0.94, $\gamma_{\overline{P}_d}$ declines from 22.9 to 19.3, $\eta_{\overline{P}_d}$ declines from 62.95% to 54.65%, a decline of 13.19%. When only HTL exists, comparing curves 1 and 3, as B grows from 0 W/K to 2.2 W/K, $\eta_{\overline{P}_d}$ declines from 62.95% to 58.34%, a decline of 7.32%. When μ, η_c and η_e exist, comparing curves 1 and 2′, as μ grows from 0 kg/s to 1.2 kg/s, and the η_c and η_e decline from 1 to 0.94, $\gamma_{\overline{P}_d}$ declines from 22.9 to 19.3, $\eta_{\overline{P}_d}$ declines from 62.95% to 53.74%, a decline of 14.63%. When FL and HTL exist, comparing curves 1 and 4, as μ grows from 0 kg/s to 1.2 kg/s, and B grows from 0 W/K to 2.2 W/K, $\eta_{\overline{P}_d}$ declines from 62.95% to 57.49%, a decline of 8.67%. When IIL and HTL exist, comparing curves 1 and 3′, as η_c and η_e decline from 1 to 0.94, the B grows from 0 W/K to 2.2 W/K, $\gamma_{\overline{P}_d}$ declines from 22.9 to 19.3, $\eta_{\overline{P}_d}$ declines from 62.95% to 50.71%, a decline of 19.44%. When FL, HTL and IIL exist, comparing curves 1 and 4′, as μ grows from 0 kg/s to 1.2 kg/s, the B grows from 0 W/K to 2.2 W/K, and the η_c and η_e decline from 1 to 0.94, $\gamma_{\overline{P}_d}$ declines from 22.9 to 19.3, $\eta_{\overline{P}_d}$ declines from 62.95% to 49.86%, a decline of 20.79%. As the specific heat of the working fluid changes more violently with temperature and the three losses increase, the thermal efficiency in the circumstances of maximum dimensionless power density decreases.

Figure 4 shows the variation in maximum-specific volume ratio (v_1/v_s), η and maximum pressure ratio (p_3/p_1) with τ in the circumstances of $\overline{P}_{\max}$ and $(\overline{P}_d)_{\max}$. Figure 4a shows the v_1/v_s, where v_1 is the maximum-specific volume, v_s is the stroke volume, and the larger the v_1/v_s, the larger the volume of the engine. Figure 4c shows the p_3/p_1, p_3 is the maximum pressure of the cycle, p_1 is the minimum pressure of the cycle, the larger the p_3/p_1, the higher the internal pressure of the engine, and the higher the requirements for engine materials.

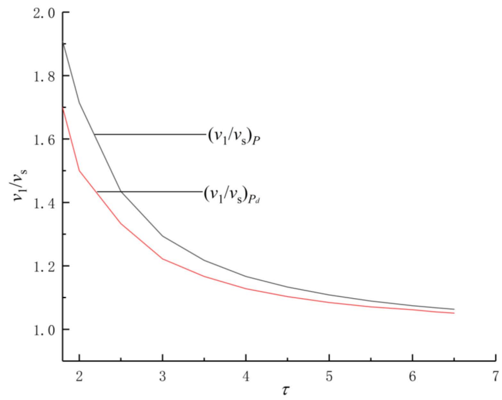

(**a**)

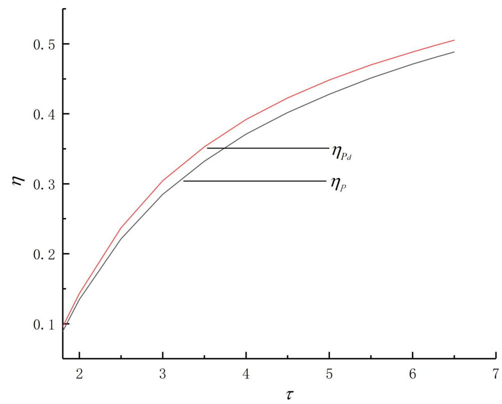

(**b**)

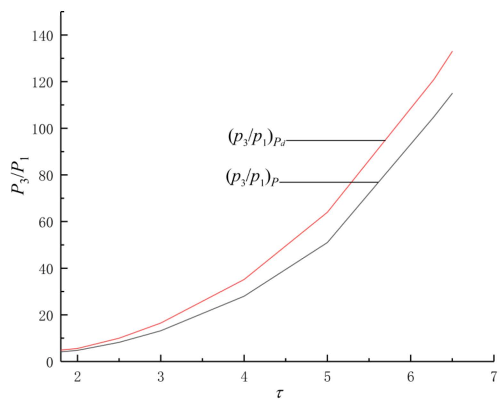

(**c**)

Figure 4. Various variations in v_1/v_s, η and p_3/p_1 with τ. (**a**) v_1/v_s with τ. (**b**) η with τ. (**c**) p_3/p_1 with τ.

The v_1/v_s corresponding to $\overline{P}_{\max}$ is always larger than v_1/v_s corresponding to $(\overline{P}_d)_{\max}$, the p_3/p_1 corresponding to $(\overline{P}_d)_{\max}$ is always larger than the p_3/p_1 ratio corresponding to $\overline{P}_{\max}$ and $\eta_{\overline{P}_d}$ is always higher than $\eta_{\overline{P}}$. Compared with $\overline{P}_{\max}$, the cycle in the circumstances of $(\overline{P}_d)_{\max}$ is smaller and more efficient.

3.2. Ecological Function Analyses and Optimizations

Figure 5 shows the effects of cycle parameters on the $\overline{E}$ and γ ($\overline{E}-\gamma$) as well as the $\overline{E}$ and η ($\overline{E}-\eta$) characteristics. It can be seen that the $\overline{E}-\gamma$ is parabolic-like one, and the maximum ecological function ($\overline{E}_{\max}$) corresponds to a γ of $\gamma_{\overline{E}}$.The $\overline{E}-\eta$ is loop-shaped one, and there is an $\overline{E}_{\max}$ operating point and an $\eta_{\max}$ operating point in the cycle As seen in Figure 5a,b, as τ grows, both $\gamma_{\overline{E}}$ and $\eta_{\overline{E}}$ get larger. When τ grows from 5.78 to 6.78, $\gamma_{\overline{E}}$ grows from 25.8 to 37.1, $\eta_{\overline{E}}$ grows from 0.5086 to 0.5450 and $\eta_{\overline{E}}$ grows by about 7.16%. As seen in Figure 5c,d, as ρ grows, both $\gamma_{\overline{E}}$ and $\eta_{\overline{E}}$ get larger. When ρ grows from 1.2 to 1.6, $\gamma_{\overline{E}}$ grows from 33.5 to 43.6, $\eta_{\overline{E}}$ grows from 0.5303 to 0.5634 and $\eta_{\overline{E}}$ grows by about 3.37%. With the increase in the temperature ratio and pre-expansion ratio, the compression ratio and thermal efficiency in the circumstances of maximum dimensionless ecological function increase.

Figure 6 shows the $E-P$ and $E-\eta$ curves with varying losses and SH characteristics. Figure 6a,c and e show that, except at the $P_{\max}$ point, corresponding to any E of the cycle, the P has two different values. The E of the cycle decreases with increasing μ, B, η_c and η_e. Curve 1 in Figure 6f is reversible without any loss, and the curve is a parabolic-like one, whereas the others are loop-shaped. Each E value (except the maximum value point) corresponds to two η values. The heat engine should be run in the circumstances with a higher η during actual operation. Figure 6a–d show the effects of SH of WF characteristics on cycle performance. Among them, curve 1 is the $E-P$ of the heat engine and the $E-\eta$ under the conditions of constant SH of WF. Under certain conditions of ecological function, the PM heat engine should be run at a larger power output during actual operation. As the specific heat of the working fluid changes more violently with temperature and the three losses decrease, the ecological function, power output and thermal efficiency will all increase.

Figure 7 shows the relationship between P and η characteristics under different OOs. Through numerical calculations, the $P_{\max}$, $\eta_{\max}$, P in the circumstances of $\eta_{\max}$ (P_η), P in the circumstances of $\overline{E}_{\max}$ (P_E), P in the circumstances of $(\overline{P}_d)_{\max}$ (P_{p_d}), η in the circumstances of $P_{\max}$ (η_P), η in the circumstances of $(\overline{P}_d)_{\max}$ (η_{p_d}), and η in the circumstances of $E_{\max}$ (η_E) can be obtained. Both P and η decline with the increases of μ, and $P_{\max}>P_{p_d}>P_E>P_\eta$, $\eta_{\max}>\eta_E>\eta_{p_d}>\eta_P$. Numerical calculations show that when the μ is $1.2 kg/s$, $P_{\max}$ is 20162 W, P_{p_d} is 20049 W, P_E is 18904 W, P_η is 16725 W, $\eta_{\max}$ is 0.5383 W, η_{p_d} is 0.4986 W, η_E is 0.5280, and η_P is 0.4811. Compared with $P_{\max}$, P_{p_d} decreased by about 0.56%, P_E decreased by about 6.23%, and P_η decreased by about 17.05%. Compared with $\eta_{\max}$, η_{p_d} decreased by about 7.38%, η_E decreased by about 1.91%, η_P decreased by about 10.63%. Compared with $E_{\max}$, P_{p_d} decreased by about 5.71%, η_{p_d} increased by about 5.57%. P_{p_d} and P_E are higher than P_η, η_E and η_{p_d} are higher than η_P, P_{p_d} is higher than P_E and η_E is higher than η_{p_d}. The ecological function objective function reflects the compromise between power output and efficiency.

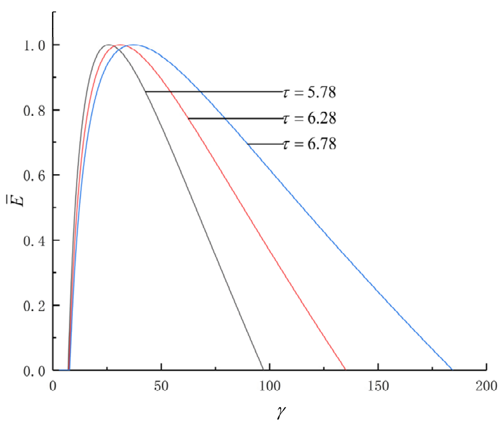

(a)

Figure 5. *Cont.*

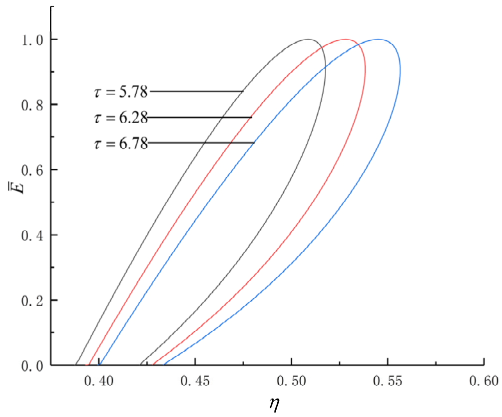

(**b**)

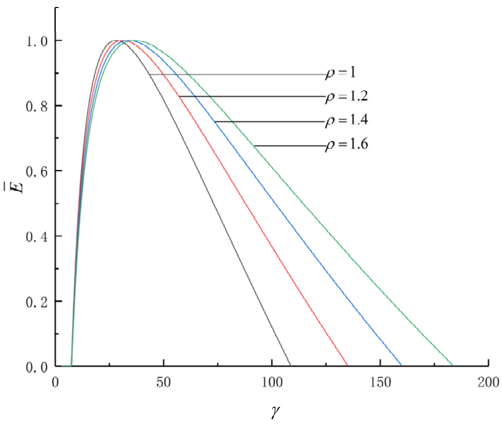

(**c**)

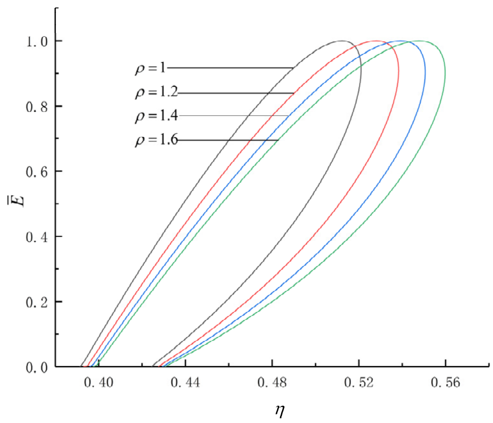

(**d**)

Figure 5. The effects of τ and ρ on $\overline{E} - \gamma$ and $\overline{E} - \eta$. (**a**) Effect of τ on $\overline{E} - \gamma$. (**b**) Effect of τ on $\overline{E} - \eta$. (**c**) Effect of ρ on $\overline{E} - \gamma$. (**d**) Effect of ρ on $\overline{E} - \eta$.

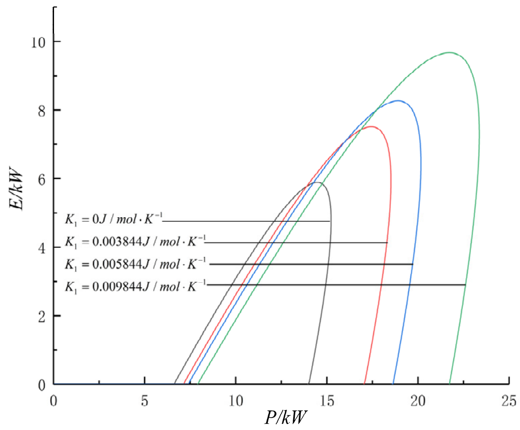

(**a**)

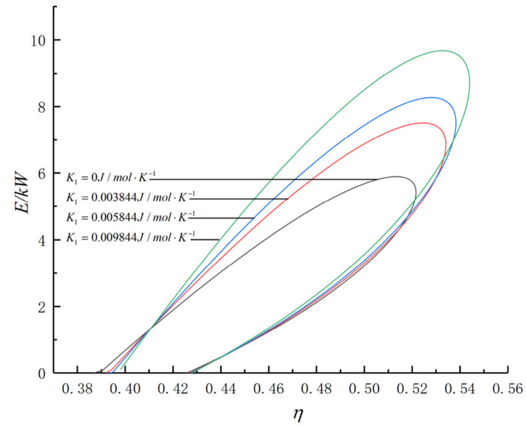

(**b**)

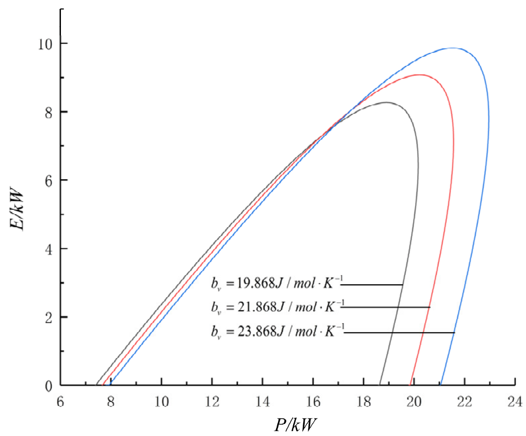

(**c**)

Figure 6. *Cont*.

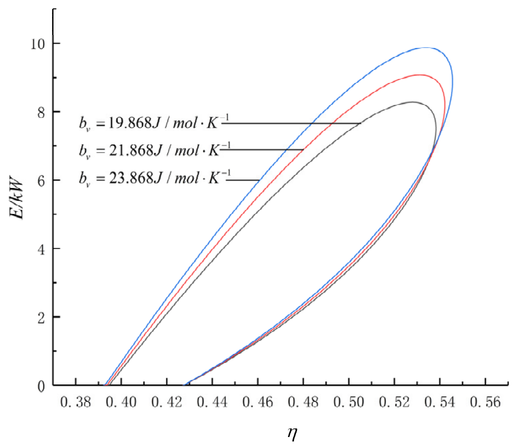

(**d**)

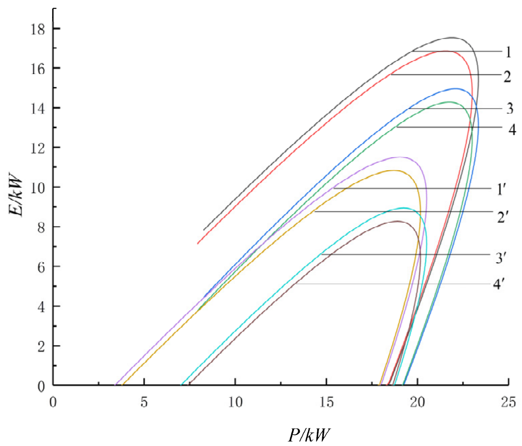

(**e**)

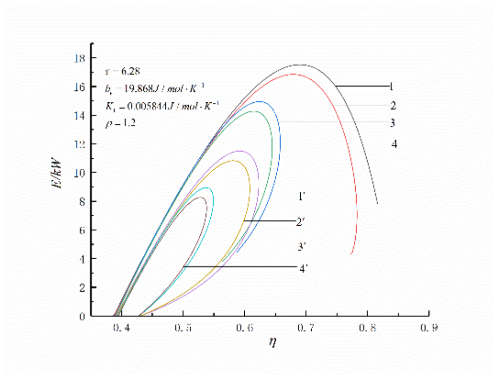

(**f**)

Figure 6. Effects of k_1, b_v, B, μ, η_c η_e on $\overline{P}_d - \gamma$ and $\overline{P}_d - \eta$. (**a**) Effect of k_1 on $E - P$. (**b**) Effect of k_1 on $E - \eta$. (**c**) Effect of b_v on $E - P$. (**d**) Effect of b_v on $E - \eta$. (**e**) $E - P$. (**f**) $E - \eta$.

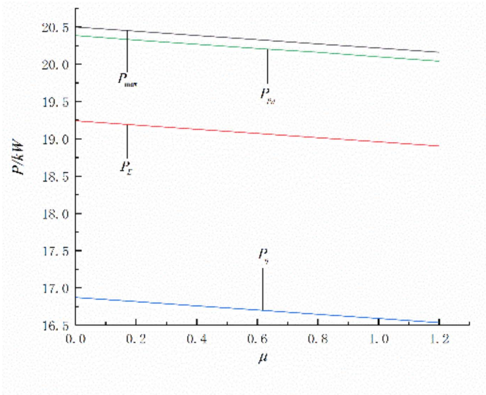

(**a**)

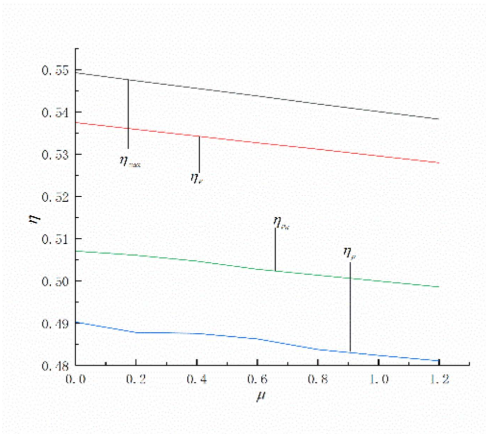

(**b**)

Figure 7. P and η in the circumstances of different objective functions. (**a**) P. (**b**) η.

4. Multi-Objective Optimizations

With the increase in cycle OOs, the optimization of the cycle sometimes needs to take into account MOO. However, MOO cannot make many OOs achieve the highest value simultaneously. The finest compromise can be obtained by weighing the advantages and disadvantages of MOO. The NSGA-II (Figure 8 is the flow chart of the arithmetic) is applied herein, γ is taken as the optimization variables, and the $\overline{P}_d$, $\overline{P}$, η and $\overline{E}$ are taken as OOs, and one-, two-, three- and four-objective optimizations are performed. Three decision-making methods, LINMAP [90], TOPSIS [91,92] and Shannon Entropy [93], are used to select the reasonable solution, and the average distances (i.e., deviation index) [94] between Pareto frontier and positive or negative ideal point are compared, and the reasonable solution is obtained.

The deviation index is [94]

$$D = \frac{\sqrt{\sum_{j=1}^{m} \left(G_j - G_j^{\text{positive}}\right)^2}}{\sqrt{\sum_{j=1}^{m} \left(G_j - G_j^{\text{positive}}\right)^2} + \sqrt{\sum_{j=1}^{m} \left(G_j - G_j^{\text{negative}}\right)^2}} \tag{32}$$

where G_j is the j-th optimization objective, G_j^{positive} is the j-th optimization objective of the positive ideal point and G_j^{negative} is the j-th optimization objective of the negative ideal point.

Figure 9 shows the Pareto fronts for MOO, including six two-objective optimizations, four three-objective optimizations, and one four-objective optimization. Table 1 lists the numerical results. As seen in Figure 9a–f, as $\overline{P}$ grows, η, $\overline{E}$, and $\overline{P}_d$ decline. As η grows, $\overline{P}_d$

and $\overline{E}$ decline. As $\overline{E}$ grows, $\overline{P}_d$ declines. It can be seen from Table 1 that when $\overline{E}$ and $\overline{P}_d$ serve as the OOs, the DI obtained by the LINMAP is smaller. When $\overline{P}$ and η or $\overline{P}$ and $\overline{E}$ or η and $\overline{P}_d$ serve as the OOs, the DI obtained by the TOPSIS is smaller. When $\overline{P}$ and $\overline{P}_d$ or η and $\overline{E}$ serve as OOs, the DI obtained by the Shannon Entropy is smaller. In the two-objective optimization, when $\overline{P}$ and η serve as OOs, the DI obtained is the smallest. Figure 10a shows the average spread and generation number of $\overline{P}-\eta$ in the circumstances of two-objective optimization. The arithmetic converged at generation 395, and the DI is 0.128.

Table 1. Results of one-, two-, three- and four-objective optimizations.

Optimization Schemes	Solutions	Optimization Variable	Optimization Objectives				Deviation Index
		γ	$\overline{P}$	η	$\overline{E}$	$\overline{P}_d$	D
Four-objective optimization ($\overline{P},\eta,\overline{E}and\overline{P}_d$)	LINMAP	25.9430	0.9664	0.5188	0.9844	0.9855	0.1367
	TOPSIS	26.2119	0.9650	0.5194	0.9861	0.9845	0.1380
	Shannon Entropy	19.2876	0.9944	0.4896	0.8914	1.0000	0.3216
Three-objective optimization ($\overline{P}$, η and $\overline{E}$)	LINMAP	26.9262	0.9612	0.5209	0.9902	0.9816	0.1443
	TOPSIS	26.9262	0.9612	0.5209	0.9902	0.9816	0.1443
	Shannon Entropy	31.1234	0.9374	0.5281	1.0000	0.9623	0.2137
Three-objective optimization ($\overline{P}$, η and $\overline{P}_d$)	LINMAP	24.9370	0.9715	0.5165	0.9769	0.9891	0.1365
	TOPSIS	24.0989	0.9756	0.5144	0.9691	0.9918	0.1448
	Shannon Entropy	19.2843	0.9944	0.4986	0.8913	1.0000	0.3212
Three-objective optimization ($\overline{P}$, $\overline{E}$ and $\overline{P}_d$)	LINMAP	25.1910	0.9703	0.5171	0.9789	0.9882	0.1355
	TOPSIS	25.4641	0.9689	0.5177	0.9810	0.9872	0.1353
	Shannon Entropy	19.2680	0.9945	0.4985	0.8909	1.0000	0.3220
Three-objective optimization (η, $\overline{E}$ and $\overline{P}_d$)	LINMAP	28.1169	0.9547	0.5232	0.9952	0.9766	0.1602
	TOPSIS	28.1169	0.9547	0.5232	0.9952	0.9766	0.1602
	Shannon Entropy	19.2876	1.0000	0.4986	0.8914	1.0000	0.3173
Two-objective optimization ($\overline{P}$ and η)	LINMAP	25.3246	0.9696	0.5174	0.9800	0.9877	0.1353
	TOPSIS	27.7548	0.9724	0.5160	0.9939	0.9781	0.1281
	Shannon Entropy	25.5246	0.8285	0.5383	0.9815	0.9870	0.4126
Two-objective optimization ($\overline{P}$ and $\overline{E}$)	LINMAP	25.5543	0.9684	0.5179	0.9817	0.9869	0.1379
	TOPSIS	25.8498	0.9669	0.5186	0.9838	0.9858	0.1361
	Shannon Entropy	31.0929	0.9376	0.5280	1.0000	0.9625	0.2131
Two-objective optimization ($\overline{P}$ and $\overline{P}_d$)	LINMAP	17.5388	0.9984	0.4908	0.8437	0.9985	0.4170
	TOPSIS	17.5606	0.9984	0.4909	0.8444	0.9986	0.4157
	Shannon Entropy	19.2810	0.9944	0.4986	0.8912	1.0000	0.2934
Two-objective optimization (η and $\overline{E}$)	LINMAP	34.8168	0.9151	0.5324	0.9941	0.9427	0.2896
	TOPSIS	34.5448	0.9168	0.5321	0.9949	0.9949	0.2336
	Shannon Entropy	31.1076	0.9375	0.5281	1.0000	0.9624	0.2134
Two-objective optimization (η and $\overline{P}_d$)	LINMAP	27.7515	0.9567	0.5225	0.9938	0.9782	0.1549
	TOPSIS	27.1475	0.9600	0.5214	0.9912	0.9807	0.1469
	Shannon Entropy	19.2652	0.9945	0.4985	0.8909	1.0000	0.3220
Two-objective optimization ($\overline{E}$ and $\overline{P}_d$)	LINMAP	26.6256	0.9628	0.5203	0.9886	0.9828	0.1413
	TOPSIS	26.8632	0.9616	0.5208	0.9898	0.9819	0.1435
	Shannon Entropy	19.2744	0.9945	0.4985	0.8911	1.0000	0.3216
Maximum of $\overline{P}$	——	15.7438	1.0000	0.4813	0.7788	0.9932	0.5135
Maximum of η	——	48.1678	0.8310	0.5383	0.9106	0.8631	0.6195
Maximum of $\overline{E}$	——	31.1146	0.9375	0.5280	1.0000	0.9624	0.2134
Maximum of $\overline{P}_d$	——	19.3173	0.9943	0.4987	0.8921	1.0000	0.3194
Positive ideal point		——	1.0000	0.5383	1.0000	1.0000	——
Negative ideal point		——	0.8287	0.4812	0.8000	0.8608	——

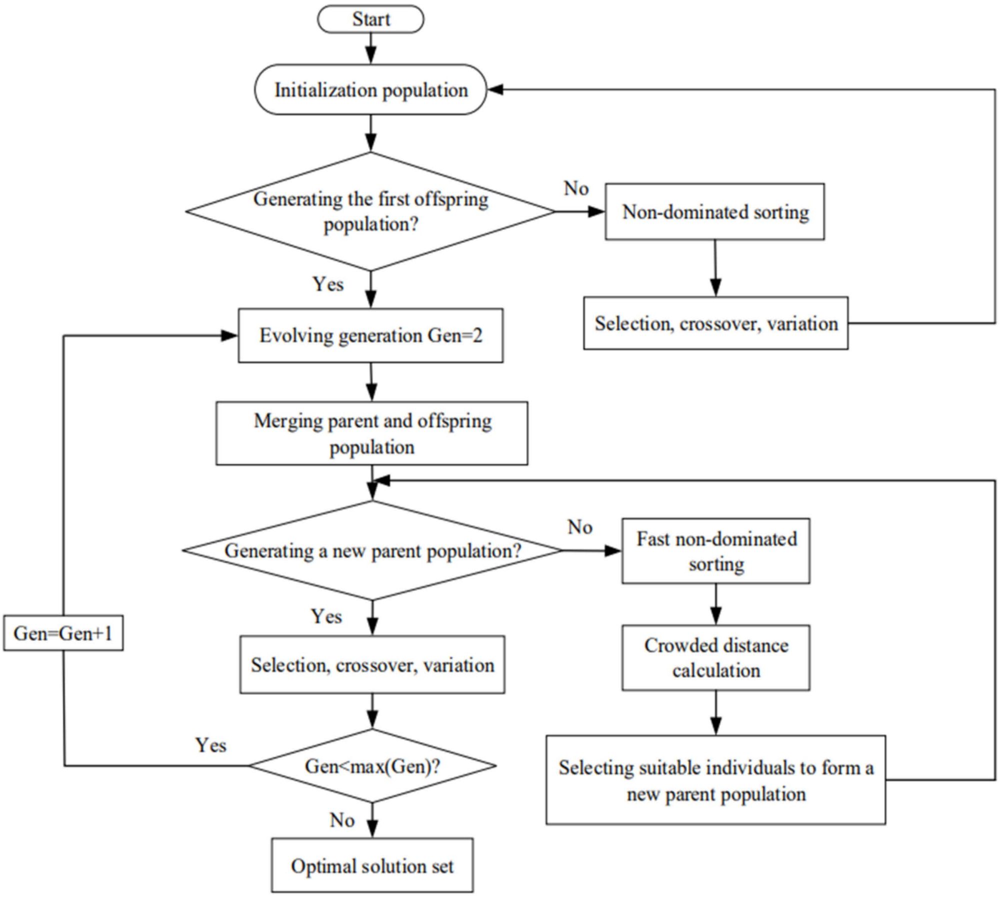

Figure 8. Flow diagram of NSGA-II.

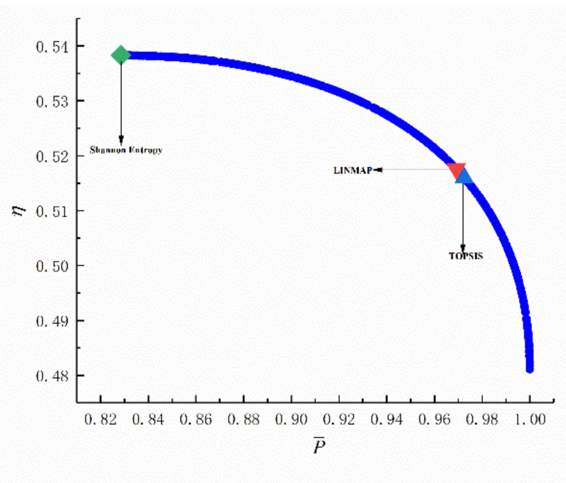

(**a**)

Figure 9. *Cont.*

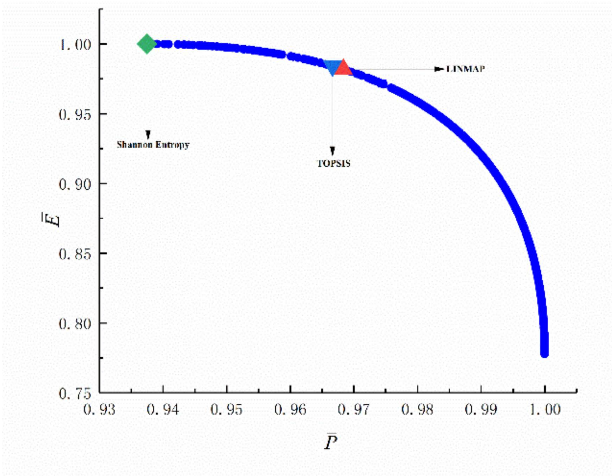

(**b**)

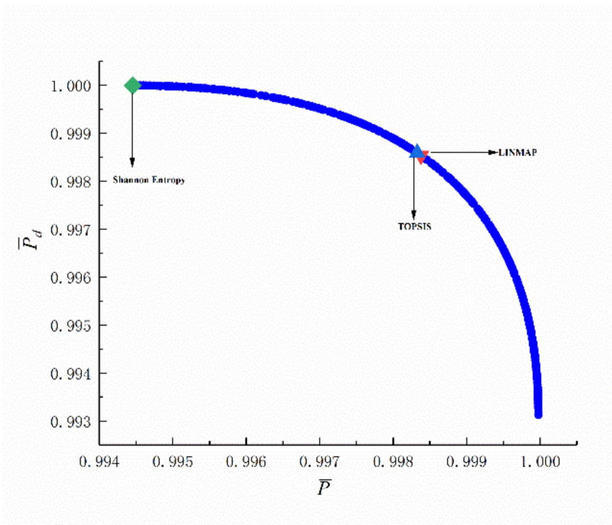

(**c**)

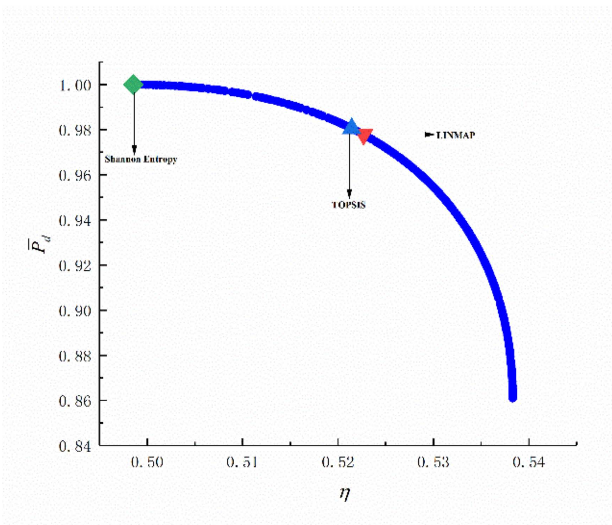

(**d**)

Figure 9. *Cont.*

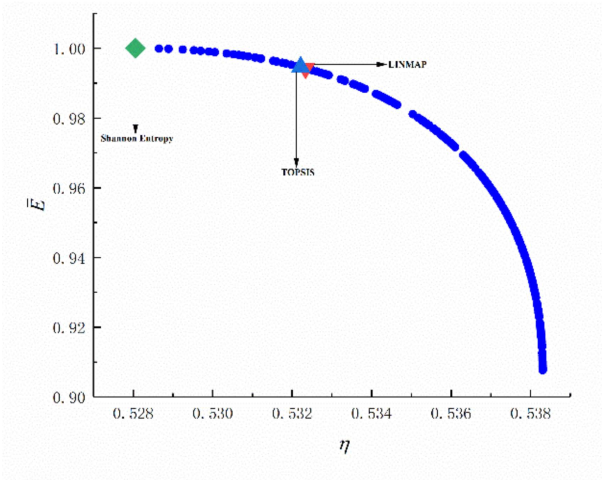

(**e**)

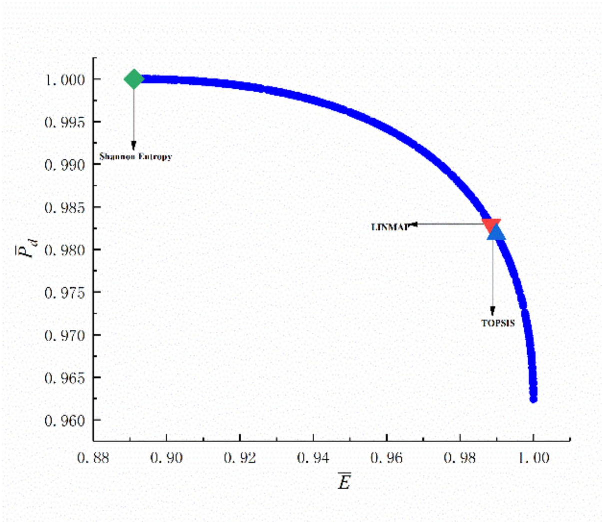

(**f**)

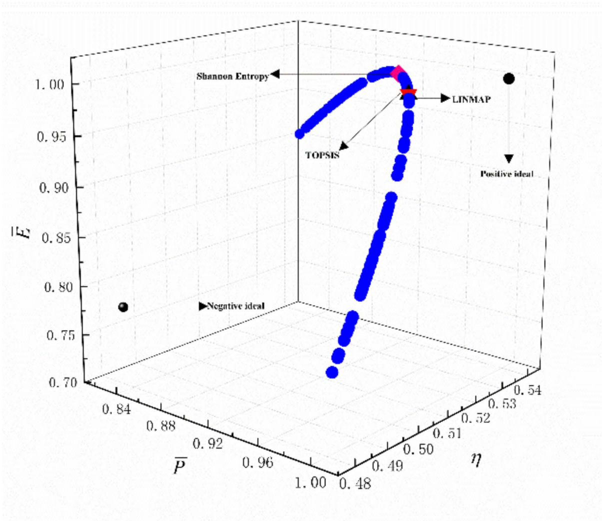

(**g**)

Figure 9. *Cont.*

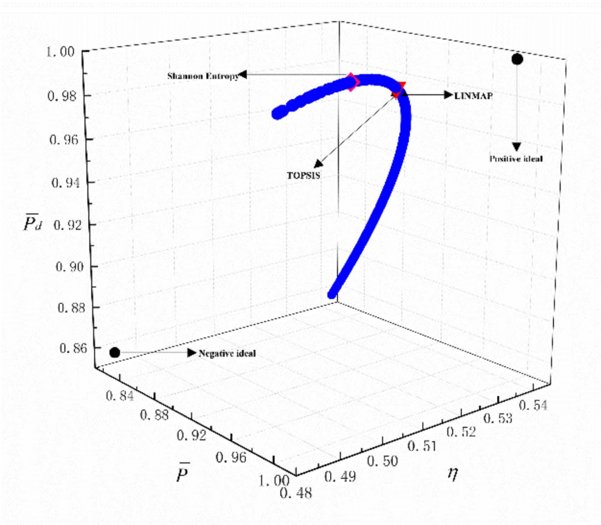

(**h**)

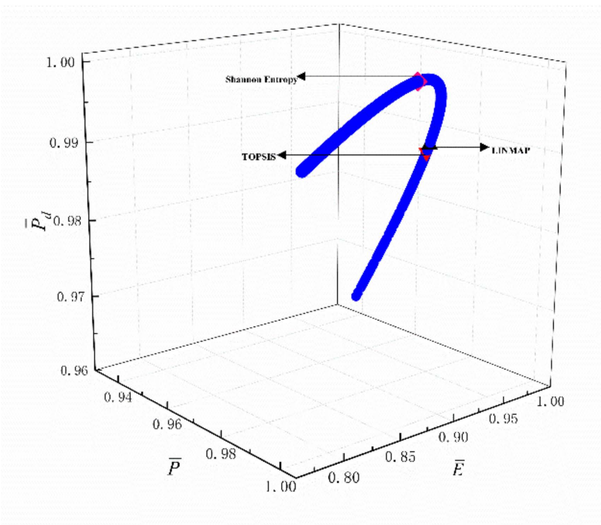

(**i**)

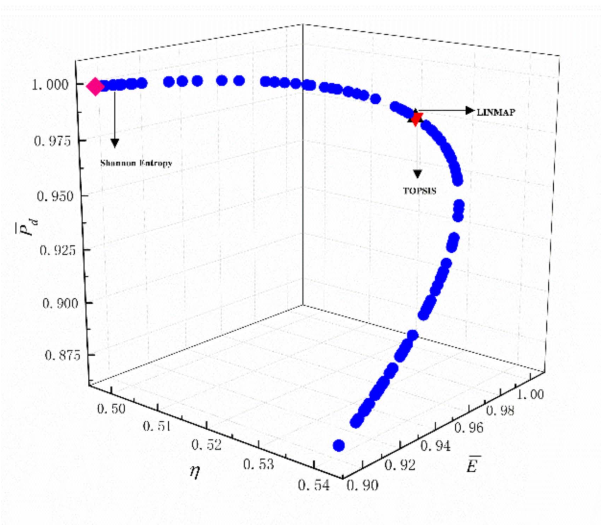

(**j**)

Figure 9. *Cont.*

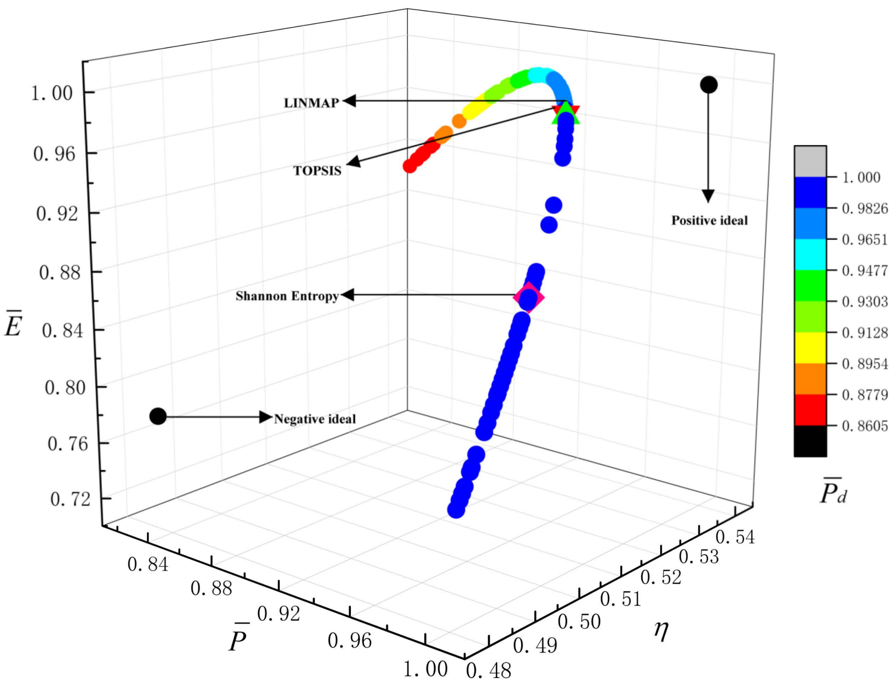

(**k**)

Figure 9. Multi-objective optimization results. (**a**) Two-objective optimization on $\overline{P} - \eta$. (**b**) Two-objective optimization on $\overline{P} - \overline{E}$. (**c**) Two-objective optimization on $\overline{P} - \overline{P}_d$. (**d**) Two-objective optimization on $\eta - \overline{P}_d$. (**e**) Two-objective optimization on $\eta - \overline{E}$. (**f**) Two-objective optimization on $\overline{E} - \overline{P}_d$. (**g**) Three-objective optimization on $\overline{P} - \eta - \overline{E}$. (**h**) Three-objective optimization on $\overline{P} - \eta - \overline{P}_d$. (**i**) Three-objective optimization on $\overline{P} - \overline{E} - \overline{P}_d$. (**j**) Three-objective optimization on $\eta - \overline{E} - \overline{P}_d$. (**k**) Four-objective optimization on $\overline{P} - \eta - \overline{E} - \overline{P}_d$.

As seen in Figure 9g,h, as $\overline{P}$ grows, η declines, $\overline{E}$ and $\overline{P}_d$ first grow and then decline. As seen in Figure 9i, as $\overline{P}$ grows, $\overline{E}$ declines, and $\overline{P}_d$ first grows and then declines. As seen in Figure 9j, as η grows, $\overline{P}_d$ declines, and $\overline{E}$ grows first and then declines. It can be seen from Table 1 that when $\overline{P}$, η and $\overline{P}_d$ serve as OOs, the DI obtained by LINMAP is smaller. When $\overline{P}$, $\overline{E}$ and $\overline{P}_d$ serve as OOs, the DI obtained by TOPSIS is smaller. When $\overline{P}$, η and $\overline{E}$ or η, $\overline{E}$ and $\overline{P}_d$ serve as OOs, the DI obtained by the LINMAP and TOPSIS are the same, and both are smaller than the DI obtained by the Shannon Entropy.

In the three-objective optimization, when $\overline{P}$, $\overline{E}$ and $\overline{P}_d$ serve OOs, the DI is the smallest. Figure 10b shows the average spread and generation number of $\overline{P} - \overline{E} - \overline{P}_d$ in the circumstances of three-objective optimization. The arithmetic converged at generation 344 and the DI is 0.1353.

As seen in Figure 9k, as $\overline{P}$ grows, η declines, $\overline{P}_d$ grows, and $\overline{E}$ grows first and then declines. The DI obtained by the LINMAP is smaller. Figure 10c shows the average spread and generation number of $\overline{P} - \eta - \overline{E} - \overline{P}_d$ in the circumstances of four-objective optimization. The arithmetic converged at generation 304, and the DI is 0.1367.

It can be seen from Table 1 that when single-objective optimizations are carried out in the circumstances of $P_{\max}$, $\eta_{\max}$, $\overline{E}_{\max}$ and $(\overline{P}_d)_{\max}$, respectively, the DI are 0.5448, 0.2897, 0.1960 and 0.2108, respectively, which are all larger than the best DI 0.1419 obtained in the four-objective optimization, which indicates that MOO produces better results.

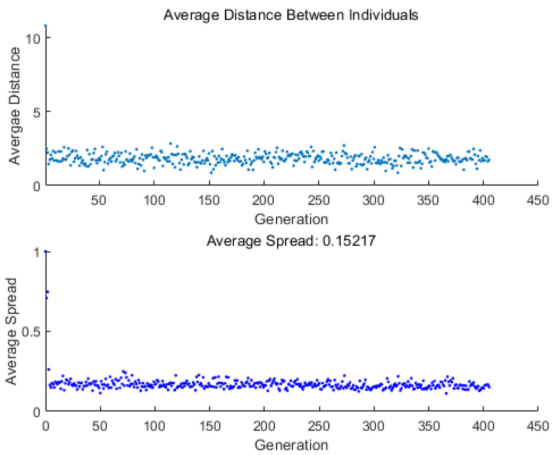

(**a**)

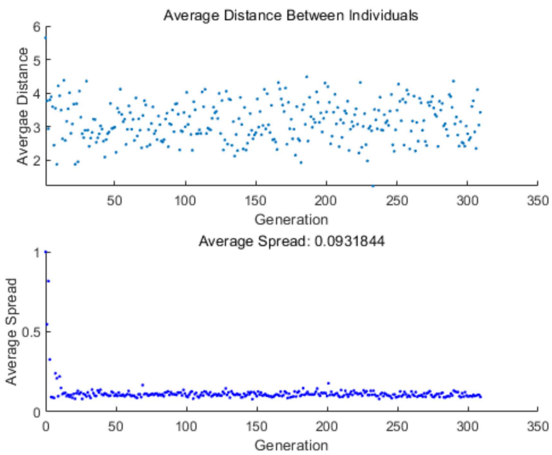

(**b**)

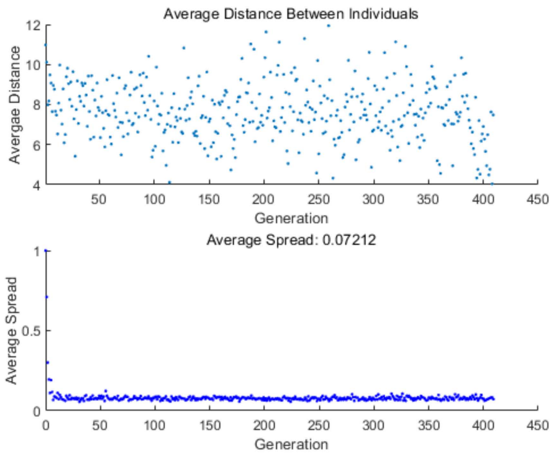

(**c**)

Figure 10. Average distance generation and average spread generation. (**a**) Average spread and generation number of $\overline{P} - \eta$. (**b**) Average spread and generation number of $\overline{P} - \overline{E} - \overline{P}_d$. (**c**) Average spread and generation number of $\overline{P} - \eta - \overline{E} - \overline{P}_d$.

5. Conclusions

Considering the linear variable SH characteristics of the WF, the optimal performance of irreversible PM cycle is studied with P_d and E as the OOs in this paper. The effects of the parameters of the cycle on the P_d and the E are analyzed; the corresponding η, v_1/v_s and p_3/p_1 of the cycle under the conditions of $(P_d)_{\max}$ and $P_{\max}$ are compared; and the corresponding P and η of the cycle under the conditions of $P_{\max}$, $\eta_{\max}$, $(\overline{P}_d)_{\max}$, and $E_{\max}$ are compared. The four OOs of the irreversible PM cycle are optimized with one-, two-, three- and four-objectives, respectively. The results show that:

1. The $\overline{P}_d - \gamma$ and $\overline{P}_d - \eta$ curves of the cycle are parabolic-like and loop-shaped, respectively. As the temperature ratio and pre-expansion ratio increase, three losses decrease and the specific heat of the working fluid changes more violently with temperature, the compression ratio and thermal efficiency in the circumstances of maximum dimensionless power density increase.
2. The $\overline{E} - \gamma$ and $E - P$ curves of the cycle are parabolic-like and the $E - \eta$ curves of the cycle are loop-shaped. As the temperature ratio and pre-expansion ratio increase, the compression ratio and thermal efficiency in the circumstances of maximum dimensionless ecological function increase. As three losses decrease and the specific heat of the working fluid changes more violently with temperature, the ecological function, power output and thermal efficiency increase.
3. Compared with the $\overline{P}_{\max}$ condition, the cycle in the circumstances of $(\overline{P}_d)_{\max}$ is smaller and more efficient.
4. The DI obtained in one-objective optimization is larger than the optimal DI obtained in MOO, indicating that the MOO results are better. Comparing the results obtained by one-, two-, three- and four-objective optimization, the MOO corresponding to the double-objective optimization $\overline{P} - \eta$ is the smallest, and its design scheme is the most ideal.
5. Variable SH characteristics of the WF always exist. It is necessary to study its effects on the MOO performances of irreversible PM cycles.

Author Contributions: Conceptualization, L.C.; Data curation, Y.G.; Funding acquisition, L.C.; Methodology, P.Z., L.C., Y.G., S.S. and H.F.; Software, P.Z., Y.G., S.S. and H.F.; Supervision, L.C.; Validation, P.Z., Y.G., S.S. and H.F.; Writing—original draft preparation, P.Z. and L.C.; Writing—reviewing and editing, L.C. All authors have read and agreed to the published version of the manuscript.

Funding: This work is supported by the National Natural Science Foundation of China (Project Nos. 52171317 and 51779262) and Graduate Innovative Fund of Wuhan Institute of Technology (Project No. CX2021044).

Acknowledgments: The authors wish to thank the reviewers for their careful, unbiased and constructive suggestions, which led to this revised manuscript.

Conflicts of Interest: The authors declare no conflict of interest.

Nomenclature

B	Heat transfer loss coefficient (W/K)
C_v	Specific heat at constant volume (J/(mol·K))
E	Ecological function (W/K)
k	Adiabatic index (-)
$\dot{m}$	Molar flow rate (mol/s)
P	Power output (W)
P_d	Power density (W/m^3)
$\dot{Q}$	Heat transfer rate (W)
R	Gas constant (J/mol/K)
T	Temperature (K)

Greek symbols	
γ	Compression ratio (-)
η	Thermal efficiency (-)
η_c	Compression efficiency (-)
η_e	Expansion efficiency (-)
μ	Friction loss coefficient (kg/s)
σ	Entropy generation rate (W/K)
ρ	Pre-expansion ratio (-)
τ	Temperature ratio (-)
Subscripts	
in	Input
$leak$	Heat leak
out	Output
max	Maximum value
P	Max power output condition
η	Max thermal efficiency condition
P_d	Max power density condition
E	Max ecological function
1–5	State points
Superscripts	
$-$	Dimensionless
Abbreviations	
DI	Deviation index
FL	Friction loss
FTT	Finite time thermodynamics
HTL	Heat transfer loss
IIL	Internal irreversibility loss
MOO	Multi-objective optimization
OO	Optimization objective
PM	Porous medium
SH	Specific heats
WF	Working fluid

References

1. Andresen, B. *Finite-Time Thermodynamics*; University of Copenhagen: Copenhagen, Denmark, 1983.
2. Bejan, A. Entropy generation minimization: The new thermodynamics of finite-size devices and finite-time processes. *J. Appl. Phys.* **1996**, *79*, 1191–1218. [CrossRef]
3. Andresen, B. Current trends in finite-time thermodynamics. *Angew. Chem. Int. Ed.* **2011**, *50*, 2690–2704. [CrossRef]
4. Kaushik, S.C.; Tyagi, S.K.; Kumar, P. *Finite Time Thermodynamics of Power and Refrigeration Cycles*; Springer: New York, NY, USA, 2017. [CrossRef]
5. Feidt, M.; Costea, M. Progress in Carnot and Chambadal modeling of thermomechanical engine by considering entropy and heat transfer entropy. *Entropy* **2019**, *21*, 1232. [CrossRef]
6. Berry, R.S.; Salamon, P.; Andresen, B. How it all began. *Entropy* **2020**, *22*, 908. [CrossRef]
7. Yasunaga, T.; Fontaine, K.; Ikegami, Y. Performance evaluation concept for ocean thermal energy conversion toward standardization and intelligent design. *Energies* **2021**, *14*, 2336. [CrossRef]
8. Costea, M.; Petrescu, S.; Feidt, M.; Dobre, C.; Borcila, B. Optimization modeling of irreversible Carnot engine from the perspective of combining finite speed and finite time analysis. *Entropy* **2021**, *23*, 504. [CrossRef] [PubMed]
9. Li, Z.; Cao, H.; Yang, H.; Guo, J. Comparative assessment of various low-dissipation combined models for three-terminal heat pump systems. *Entropy* **2021**, *23*, 513. [CrossRef]
10. Chattopadhyay, P.; Mitra, A.; Paul, G.; Zarikas, V. Bound on efficiency of heat engine from uncertainty relation viewpoint. *Entropy* **2021**, *23*, 439. [CrossRef] [PubMed]
11. Sieniutycz, S. *Complexity and Complex Chemo-Electric Systems*; Elsevier: Amsterdam, The Netherlands, 2021.
12. Chen, Y.R. Maximum profit configurations of commercial engines. *Entropy* **2011**, *13*, 1137–1151. [CrossRef]
13. Boykov, S.; Andresen, B.; Akhremenkov, A.A.; Tsirlin, A.M. Evaluation of irreversibility and optimal organization of an integrated multi-stream heat exchange system. *J. Non-Equilib. Thermodyn.* **2020**, *45*, 155–171. [CrossRef]
14. Masser, R.; Hoffmann, K.H. Optimal control for a hydraulic recuperation system using endoreversible thermodynamics. *Appl. Sci.* **2021**, *11*, 5001. [CrossRef]
15. Paul, R.; Hoffmann, K.H. Cyclic control optimization algorithm for Stirling engines. *Symmetry* **2021**, *13*, 873. [CrossRef]
16. Badescu, V. Maximum work rate extractable from energy fluxes. *J. Non-Equilib. Thermodyn.* **2022**, *47*, 77–93. [CrossRef]

17. Paul, R.; Hoffmann, K.H. Optimizing the piston paths of Stirling cycle cryocoolers. *J. Non-Equilib. Thermodyn.* **2022**, *47*, 195–203. [CrossRef]
18. Li, P.L.; Chen, L.G.; Xia, S.J.; Kong, R.; Ge, Y.L. Total entropy generation rate minimization configuration of a membrane reactor of methanol synthesis via carbon dioxide hydrogenation. *Sci. China Technol. Sci.* **2022**, *65*, 657–678. [CrossRef]
19. Paul, R.; Khodja, A.; Fischer, A.; Masser, R.; Hoffmann, K.H. Power-optimal control of a Stirling engine's frictional piston motion. *Entropy* **2022**, *24*, 362. [CrossRef] [PubMed]
20. Fischer, A.; Khodja, A.; Paul, R.; Hoffmann, K.H. Heat-only-driven Vuilleumier refrigeration. *Appl. Sci.* **2022**, *12*, 1775. [CrossRef]
21. Li, J.X.; Chen, L.G. Optimal configuration of finite source heat engine cycle for maximum output work with complex heat transfer law. *J. Non-Equilib. Thermodyn.* **2022**, *52*, 587–592. [CrossRef]
22. Smith, Z.; Pal, P.S.; Deffner, S. Endoreversible Otto engines at maximal power. *J. Non-Equilib. Thermodyn.* **2020**, *45*, 305–310. [CrossRef]
23. Ding, Z.M.; Ge, Y.L.; Chen, L.G.; Feng, H.J.; Xia, S.J. Optimal performance regions of Feynman's ratchet engine with different optimization criteria. *J. Non-Equilibrium Thermodyn.* **2020**, *45*, 191–207. [CrossRef]
24. Levario-Medina, S.; Valencia-Ortega, G.; Barranco-Jimenez, M.A. Energetic optimization considering a generalization of the ecological criterion in traditional simple-cycle and combined cycle power plants. *J. Non-Equilibrium Thermodyn.* **2020**, *45*, 269–290. [CrossRef]
25. Tang, C.Q.; Chen, L.G.; Feng, H.J.; Ge, Y.L. Four-objective optimization for an improved irreversible closed modified simple Brayton cycle. *Entropy* **2021**, *23*, 282. [CrossRef] [PubMed]
26. Ebrahimi, R. A new comparative study on performance of engine cycles under maximum thermal efficiency condition. *Energy Rep.* **2021**, *7*, 8858–8867. [CrossRef]
27. Liu, X.W.; Chen, L.G.; Ge, Y.L.; Feng, H.J.; Wu, F.; Lorenzini, G. Exergy-based ecological optimization of an irreversible quantum Carnot heat pump with spin-1/2 systems. *J. Non-Equilibrium Thermodyn.* **2021**, *46*, 61–76. [CrossRef]
28. Qiu, S.S.; Ding, Z.M.; Chen, L.G.; Ge, Y.L. Performance optimization of thermionic refrigerators based on van der Waals heterostructures. *Sci. China Technol. Sci.* **2021**, *64*, 1007–1016. [CrossRef]
29. Badescu, V. Self-driven reverse thermal engines under monotonous and oscillatory optimal operation. *J. Non-Equilib. Thermodyn.* **2021**, *46*, 291–319. [CrossRef]
30. Qi, C.Z.; Ding, Z.M.; Chen, L.G.; Ge, Y.L.; Feng, H.J. Modelling of irreversible two-stage combined thermal Brownian refrigerators and their optimal performance. *J. Non-Equilib. Thermodyn.* **2021**, *46*, 175–189. [CrossRef]
31. Valencia-Ortega, G.; Levario-Medina, S.; Barranco-Jiménez, M.A. The role of internal irreversibilities in the performance and stability of power plant models working at maximum ϵ-ecological function. *J. Non-Equilib. Thermodyn.* **2021**, *46*, 413–429. [CrossRef]
32. Qiu, S.S.; Ding, Z.M.; Chen, L.G.; Ge, Y.L. Performance optimization of three-terminal energy selective electron generators. *Sci. China Technol. Sci.* **2021**, *64*, 1641–1652. [CrossRef]
33. Ge, Y.L.; Chen, L.G.; Sun, F.R. Progress in finite time thermodynamic studies for internal combustion engine cycles. *Entropy* **2016**, *18*, 139. [CrossRef]
34. Klein, S.A. An explanation for observed compression ratios in internal combustion engines. *J. Eng. Gas Turbines Power* **1991**, *113*, 511–513. [CrossRef]
35. Angulo-Brown, F.; Fernandez, B.J.; Diaz-Pico, C.A. Compression ratio of an optimized Otto-cycle model. *Eur. J. Phys.* **1994**, *15*, 38–42. [CrossRef]
36. Angulo-Brown, F.; Rocha-Martinez, J.A.; Navarrete-Gonzalez, T.D. A non-endoreversible Otto cycle model: Improving power output and efficiency. *J. Phys. D Appl. Phys.* **1996**, *29*, 80–83. [CrossRef]
37. Chen, L.G.; Zen, F.M.; Sun, F.R. Heat transfer effects on the network output and power as function of efficiency for air standard Diesel cycle. *Energy* **1996**, *21*, 1201–1205. [CrossRef]
38. Yilmaz, T. A new performance criterion for heat engines: Efficient power. *J. Energy Inst.* **2006**, *79*, 38–41. [CrossRef]
39. Cheng, C.-Y.; Chen, C.-K. Ecological optimization of an endoreversible Brayton cycle. *Energy Convers. Manag.* **1998**, *39*, 33–44. [CrossRef]
40. Chen, L.G.; Lin, J.X.; Sun, F.R.; Wu, C. Efficiency of an Atkinson engine at maximum power density. *Energy Convers. Manag.* **1998**, *39*, 337–341. [CrossRef]
41. Zhao, Y.; Chen, J. Performance analysis and parametric optimum criteria of an irreversible Atkinson heat-engine. *Appl. Energy* **2006**, *83*, 789–800. [CrossRef]
42. Patodi, K.; Maheshwari, G. Performance analysis of an Atkinson cycle with variable specific-heats of the working fluid under maximum efficient power conditions. *Int. J. Low-Carbon Technol.* **2012**, *8*, 289–294. [CrossRef]
43. Ebrahimi, R. Effect of volume ratio of heat rejection process on performance of an Atkinson cycle. *Acta Phys. Pol. A* **2018**, *133*, 201–205. [CrossRef]
44. Wang, H.; Liu, S.; He, J. Performance analysis and parametric optimum criteria of a quantum Otto heat engine with heat transfer effects. *Appl. Therm. Eng.* **2009**, *29*, 706–711. [CrossRef]
45. Chen, L.G.; Ge, Y.L.; Liu, C.; Feng, H.J.; Lorenzini, G. Performance of universal reciprocating heat-engine cycle with variable specific heats ratio of working fluid. *Entropy* **2020**, *22*, 397. [CrossRef] [PubMed]

46. Diskin, D.; Tartakovsky, L. Efficiency at maximum power of the low-dissipation hybrid electrochemical–otto cycle. *Energies* **2020**, *13*, 3961. [CrossRef]
47. Wang, R.B.; Chen, L.G.; Ge, Y.L.; Feng, H.J. Optimizing power and thermal efficiency of an irreversible variable-temperature heat reservoir Lenoir cycle. *Appl. Sci.* **2021**, *11*, 7171. [CrossRef]
48. Bellos, E.; Lykas, P.; Tzivanidis, C. Investigation of a Solar-Driven Organic Rankine Cycle with Reheating. *Appl. Sci.* **2022**, *12*, 2322. [CrossRef]
49. Gonca, G.; Hocaoglu, M.F. Performance Analysis and Simulation of a Diesel-Miller Cycle (DiMC) Engine. *Arab. J. Sci. Eng.* **2019**, *44*, 5811–5824. [CrossRef]
50. Gonca, G.; Sahin, B. Performance analysis of a novel eco-friendly internal combustion engine cycle. *Int. J. Energy Res.* **2019**, *43*, 5897–5911. [CrossRef]
51. Gonca, G.; Sahin, B.; Genc, I. Investigation of maximum performance characteristics of seven-process cycle engine. *Int. J. Exergy* **2022**, *37*, 302–312. [CrossRef]
52. Angulo-Brown, F. An ecological optimization criterion for finite-time heat engines. *J. Appl. Phys.* **1991**, *69*, 7465–7469. [CrossRef]
53. Yan, Z.J. Comment on "Ecological optimization criterion for finite-time heat engines". *J. Appl. Phys.* **1993**, *73*, 3583. [CrossRef]
54. Chen, L.G.; Sun, F.R.; Chen, W.Z. Ecological quality factors of thermodynamic cycles. *J. Therm. Power Eng.* **1994**, *9*, 374–376. (In Chinese)
55. Gonca, G.; Genc, I. Thermoecology-based performance simulation of a Gas-Mercury-Steam power generation system (GMSPGS). *Energy Convers. Manag.* **2019**, *189*, 91–104. [CrossRef]
56. Jin, Q.; Xia, S.; Xie, T. Ecological function analysis and optimization of a recompression S-CO2 Cycle for gas turbine waste heat recovery. *Entropy* **2022**, *24*, 732. [CrossRef] [PubMed]
57. Ge, Y.L.; Chen, L.G.; Feng, H.J. Ecological optimization of an irreversible Diesel cycle. *Eur. Phys. J. Plus.* **2021**, *136*, 198. [CrossRef]
58. Ahmadi, M.H.; Pourkiaei, S.M.; Ghazvini, M.; Pourfayaz, F. Thermodynamic assessment and optimization of performance of irreversible Atkinson cycle. *Iran. J. Chem. Chem. Eng.* **2020**, *39*, 267–280.
59. Ust, Y.; Sahin, B.; Sogut, O.S. Performance analysis and optimization of an irreversible dual-cycle based on an ecological coefficient of performance criterion. *Appl. Energy* **2005**, *82*, 23–39. [CrossRef]
60. Sahin, B.; Kodal, A.; Yavuz, H. Efficiency of a Joule-Brayton engine at maximum power density. *J. Phys. D Appl. Phys.* **1995**, *28*, 1309–1313. [CrossRef]
61. Al-Sarkhi, A.; Akash, B.; Jaber, J.; Mohsen, M.; Abu-Nada, E. Efficiency of Miller engine at maximum power density. *Int. Commun. Heat Mass Transf.* **2002**, *29*, 1159–1167. [CrossRef]
62. Gonca, G.; Genc, I. Performance simulation of a double-reheat Rankine cycle mercury turbine system based on exergy. *Int. J. Exergy* **2019**, *30*, 392–403. [CrossRef]
63. Gonca, G.; Hocaoglu, M.F. Exergy-based performance analysis and evaluation of a dual-diesel cycle engine. *Thermal Sci.* **2021**, *25*, 3675–3685. [CrossRef]
64. Gonca, G.; Sahin, B. Performance investigation and evaluation of an engine operating on a modified dual cycle. *Int. J. Energy Res.* **2021**, *46*, 2454–2466. [CrossRef]
65. Al-Sarkhi, A.; Akash, B.; Abu-Nada, E. Efficiency of Atkinson engine at maximum power density using temperature dependent specific heats. *Jordan J. Mech. Ind. Eng.* **2008**, *2*, 71–75.
66. Gonca, G. Performance analysis of an Atkinson cycle engine under effective power and effective power density conditions. *Acta Phys. Pol. A.* **2017**, *132*, 1306–1313. [CrossRef]
67. Raman, R.; Kumar, N. Performance analysis of Diesel cycle under efficient power density condition with variable specific heat of working fluid. *J. Non-Equilib. Thermodyn.* **2019**, *44*, 405–416. [CrossRef]
68. Li, Y.; Liao, S.; Liu, G. Thermo-economic multi-objective optimization for a solar-dish Brayton system using NSGA-II and decision making. *Int. J. Electr. Power Energy Syst.* **2015**, *64*, 167–175. [CrossRef]
69. Chen, L.G.; Tang, C.Q.; Feng, H.J.; Ge, Y.L. Power, efficiency, power density and ecological function optimizations for an irreversible modified closed variable-temperature reservoir regenerative Brayton cycle with one isothermal heating process. *Energies* **2020**, *13*, 5133. [CrossRef]
70. Fergani, Z.; Morosuk, T.; Touil, D. Exergy-based multi-objective optimization of an organic Rankine cycle with a zeotropic mixture. *Entropy* **2021**, *23*, 954. [CrossRef] [PubMed]
71. Teng, S.; Feng, Y.-Q.; Hung, T.-C.; Xi, H. Multi-objective optimization and fluid selection of different cogeneration of heat and power systems based on organic Rankine cycle. *Energies* **2021**, *14*, 4967. [CrossRef]
72. Baghernejad, A.; Anvari-Moghaddam, A. Exergoeconomic and environmental analysis and Multi-objective optimization of a new regenerative gas turbine combined cycle. *Appl. Sci.* **2021**, *11*, 11554. [CrossRef]
73. Xie, T.; Xia, S.; Wang, C. Multi-objective optimization of Braun-type exothermic reactor for ammonia synthesis. *Entropy* **2022**, *24*, 52. [CrossRef]
74. Shi, S.S.; Chen, L.G.; Ge, Y.L.; Feng, H.J. Performance optimizations with single-, bi-, tri- and quadru-objective for irreversible Diesel cycle. *Entropy* **2021**, *23*, 826. [CrossRef] [PubMed]
75. Ge, Y.L.; Shi, S.S.; Chen, L.G.; Zhang, D.F.; Feng, H.J. Power density analysis and multi-objective optimization for an irreversible Dual cycle. *J. Non-Equilib. Thermodyn.* **2022**, *47*, 289–309. [CrossRef]

76. Wu, Q.K.; Chen, L.G.; Ge, Y.L.; Shi, S.S. Multi-objective optimization of endoreversible magnetohydrodynamic cycle. *Energy Rep.* **2022**, *8*, 8918–8927. [CrossRef]
77. Chen, L.G.; Li, P.L.; Xia, S.J.; Kong, R.; Ge, Y.L. Multi-objective optimization of membrane reactor for steam methane reforming heated by molten salt. *Sci. China Techol. Sci.* **2022**, *65*, 1396–1414. [CrossRef]
78. Deb, K.; Pratap, A.; Agarwal, S.; Meyarivan, T. A fast and elitist multiobjective genetic algorithm: NSGA-II. *IEEE Trans. Evol. Comput.* **2002**, *6*, 182–197. [CrossRef]
79. Ferrenberg, A.J. The Single cylinder regenerated internal combustion engine. SAE Technical Paper. *Earthmoving Ind. Conf. Expo.* **1990**, 1–17. [CrossRef]
80. Xie, M.Z. A new concept internal combustion engine-super adiabatic engine based on porous media combustion technology. *Re Kexue yu Jishu* **2003**, *2*, 189–194. (In Chinese)
81. Weclas, M. *Strategy for Intelligent Internal Combustion Engine with Homogenous Combustion in Cylinder*; Georg-Simon-Ohm University of Applied Sciences: Nurembreg, Germany, 2009.
82. Durst, F.; Weclas, M. A new type of internal combustion engine based on the porous-medium combustion technique. *SAGE J.* **2001**, *215*, 63–81. [CrossRef]
83. Liu, H.S.; Xie, M.Z.; Chen, S. Thermodynamic analysis of ideal cycle of porous media (PM). *J. Eng. Thermophys.* **2006**, *27*, 553–555. (In Chinese)
84. Zhao, Z.G.; Xie, M.Z. Multidimensional numerical study of combustion process of Porous Media engine. *J. Intern. Combust. Eng.* **2007**, *25*, 7–14. (In Chinese)
85. Liu, H.S.; Xie, M.Z.; Wu, D. Thermodynamic analysis of the heat regenerative cycle in porous medium engine. *Energy Convers. Manag.* **2009**, *50*, 297–303. [CrossRef]
86. Ge, Y.L.; Chen, L.G.; Sun, F.R. Thermodynamic modeling and parametric study for porous medium engine cycles. *Termotehnica* **2009**, *13*, 49–55.
87. Zang, P.C.; Ge, Y.L.; Chen, L.G.; Gong, Q.R. Power density characteristic analysis and multi-objective optimization of an irreversible porous medium engine cycle. *Case Stud. Therm. Eng.* **2022**, *35*, 102154. [CrossRef]
88. Ghatak, A.; Chakraborty, S. Effect of external irreversibilities and variable thermal properties of working fluid on thermal performance of a Dual internal combustion engine cycle. *Strojn'Icky Casopis* **2007**, *58*, 1–12.
89. Gonca, G.; Palaci, Y. Performance investigation of a Diesel engine under effective efficiency-power-power density conditions. *Sci. Iran.* **2018**, *26*, 843–855. [CrossRef]
90. Sayyaadi, H.; Mehrabipour, R. Efficiency enhancement of a gas turbine cycle using an optimized tubular recuperative heat exchanger. *Energy* **2012**, *38*, 362–375. [CrossRef]
91. Hwang, C.L.; Yoon, K. *Multiple Attribute Decision Making-Methods and Applications a State of the Art Survey*; Springer: New York, NY, USA, 1981.
92. Etghani, M.M.; Shojaeefard, M.H.; Khalkhali, A.; Akbari, M. A hybrid method of modified NSGA-II and Topsis to optimize performance and emissions of a diesel engine using biodiesel. *Appl. Therm. Eng.* **2013**, *59*, 309–315. [CrossRef]
93. Guisado, J.; Morales, F.J.; Guerra, J. Application of shannon's entropy to classify emergent behaviors in a simulation of laser dynamics. *Math. Comput. Modell.* **2005**, *42*, 847–854. [CrossRef]
94. Kumar, R.; Kaushik, S.C.; Kumar, R.; Hans, R. Multi-objective thermodynamic optimization of an irreversible regenerative Brayton cycle using evolutionary algorithm and decision making. *Ain Shams Eng. J.* **2016**, *7*, 741–753. [CrossRef]